ESO Science Archive Facility - Phase 3 Data Release Description
ESO public survey programme VHS - VISTA Hemisphere Survey, Data Release DR5
provided by Richard McMahon, submitted between 2019-11-05 and 2020-01-23, published on 2020-03-17

VISTA Hemisphere Survey Data Release

**Imaging and Catalogue Data Release 5 (DR5)**

**Data Collection:** VHS, VHS_DR5_CATALOGUES

**Release Number:** 5

**Data Provider:** Estelle Pons, Richard McMahon, Manda Banerji, Carlos Gonzalez-Fernandez and the VHS collaboration

**Date:** DD.MM.2020

**Abstract:**

The VISTA Hemisphere Survey (VHS; ESO Programme ID: 79.A-2010) is a wide field near infrared survey, which when combined with other VISTA public surveys will result in coverage of the whole southern celestial hemisphere (Declination $< 0°$; $\sim 20,000\,\mathrm{deg}^2$) to a depth 30 times fainter than 2MASS/DENIS in at least two wavebands (J and $K_s$), with a minimum exposure time of 60 seconds per waveband and a median $5\sigma$ point source depth of AB = 20.8 and 20.0 in J and $K_s$ wavebands respectively. In the South Galactic Cap, around 4500 $\mathrm{deg}^2$ is being imaged deeper with an exposure time per coadded image of 120–240 seconds in J, 120 seconds in $K_s$ and partial coverage in H band with an exposure time of 120 seconds, producing median $5\sigma$ point limits of AB = 21.4, 20.7 and 20.3 in J, H and $K_s$ respectively. In this 4500 $\mathrm{deg}^2$ region of sky deep multi-band optical (grizY) imaging data is being provided by the Dark Energy Survey (DES). The remainder of the high galactic latitude ($|b| > 30°$) sky is being imaged in Y, J, $K_s$ for 60–120 sec per band with median $5\sigma$ point source limits of AB = 21.1, 20.8 and 20.0 and partial coverage in H with a median $5\sigma$ point source limit of 20.3. This region is being imaged in the optical wavebands (ugriz) by the the VST ATLAS survey. The median $5\sigma$ point source depths for the total survey area coadd images in this data release is AB=21.1, 20.8, 20.5, 20.0 in Y, J, H and $K_s$ wavebands respectively.

This data release (DR5) contains 11370 tile level multi-band source catalogues based on 3226 Y band, 11332 J band, 1961 H band and 11326 $K_s$ band tiles derived from VHS observations taken over a 8 year period between the start of the survey (UT date of 2009 November 04) during ESO Observing Period 84 and the end of ESO Observing Period 98 (UT date of 2017 March 31). There are a total of 1,374,207,485 sources including sources detected in a single waveband. The sky coverage is 4825 $\mathrm{deg}^2$, 16689 $\mathrm{deg}^2$, 2901 $\mathrm{deg}^2$, 16684 $\mathrm{deg}^2$ in Y, J, H and $K_s$ respectively. The coverage in at least one waveband covering is 16,730 $\mathrm{deg}^2$ of sky.

In addition to the multi-band source catalogues described above, this data release contains the first public ESO release of multi-extension FITs (MEF) format pawprint image files, FITS format tile images, weight map images and single band tile source lists for observations obtained during ESO Observing periods 96 to 98 (UT date range 2015 October 1 to 2017 March 31 inclusive). The release also contains image products and single band source lists for Period 95 (date range 2015 April to 2015 Sep 30) which were previously released in data release DR4, and were reprocessed with a more recent version of the CASU pipeline software (version 1.5).

This data release contains data which has primarily been processed with version 1.5 of the CASU pipeline. Changes since version 1.3 of the CASU pipeline include an updated photometric calibration and updates to the Galactic extinction coefficients used in generating the photometric zero-points (see González-Fernández et al. (2018) for more details). In most fields the zero-point change is at the level of 1% to 2%.

## Contents

**1 Overview of Observations** **2**

**2 Release Content** **4**

**3 Release Notes** **6**

3.1 CASU pipeline version 1.3 (2013/03/27) . . . 7

3.2 CASU pipeline version 1.5 (2017/01/01) . . . 8

**4 Data Reduction and Calibration** **9**

4.1 Data processing steps . . . 9

4.2 Astrometric Calibration . . . 10

4.3 Photometric Calibration . . . 11

4.4 Star-galaxy classification . . . 12

**5 Multi-band source catalogue description** **12**

**6 Data quality** **13**

6.1 Survey Depth . . . 13

6.2 Image seeing . . . 14

6.3 Tile level spatial astrometric systematics . . . 14

6.4 Other known problems . . . 14

**7 Acknowledgements** **15**

# 1 Overview of Observations

The VISTA telescope (Sutherland et al., 2015) camera VIRCAM (Dalton et al., 2006) consists of a sparse filled mosaic of 16 2k × 2k Raytheon Mercury Cadmium Telluride (MCT) detectors with 20$\mu$m square pixels with a mean celestial scale of 0.339" per pixel. Each single observations is called a paw-print. A series of spatially contiguous pawprint observations produced an infilled contiguous image called a tile and consists of combining a sequence of six offset pawprints that fill the gaps on the sky between the individual detectors. All VHS tiles are observed with a rotator-sky angle of 180°; thus each tile covers a rectangle approximately 1.5° in Right Ascension (RA) by 1.0° in Declination. The tiling pattern used is Tile6zz as described in the VISTA Users Guide (https://www.eso.org/sci/facilities/paranal/instruments/vircam/doc/VIS-MAN-ESO-06000-0002_v101.pdf; see also the SADT manual at https://www.eso.org/sci/observing/phase2/VIRCAM/SADT_cookbook_v2.1.pdf). Each pawprint imaging sequence consists of 2 jitters with a jitter size of 20 arc secs. Normally a Jitter pattern Jitter2d or Jitter2da was used apart from during the 'Dry Run' period that preceeded the

start of the nominal survey when some other patterns were used to verify the observing strategy.

The VHS survey is divided into 3 components for survey planning and management and purposes, based on their common OB structures. These components in alphabetic order are described below with their nominal coverage as defined in the VHS survey management plan (McMahon et al, 2007):

- VHS-ATLAS ($\sim 5000\,\mathrm{deg}^2$); consists of two regions of sky, one in the north galactic cap(NGC; $\sim 2500\,\mathrm{deg}^2$) and the second in the south galactic cap ( SGC; $\sim 2500\,\mathrm{deg}^2$) to be observed in $\mathrm{YJHK_s}$ for 60 seconds per waveband.
- VHS-DES ($\sim 4500\,\mathrm{deg}^2$); a contiguous region of sky in the SGC to be observed in $\mathrm{JHK_s}$ for 120 secsonds per waveband.
- VHS-GPS ($\sim 8200\,\mathrm{deg}^2$); A region of lower galactic latitude which we define as the VHS Galactic Plane Survey (GPS) with $5^\circ < |b| < 30^\circ$ ($\sim$8200 $\mathrm{deg}^2$); excluding the VVV and VMC regions; to be observed in J and $\mathrm{K_s}$ for 60 seconds per waveband.

The spatial coverage of VHS can be divided into three contiguous regions of the celestial sphere:

1. VHS-NGC (North Galactic Cap): $b > 30^\circ$; $\delta < 0^\circ$ ($\sim 2500\,\mathrm{deg}^2$); excluding the VIKING NGP region. This is the NGC part of VHS-ATLAS. The baseline exposures of 60 seconds per band in $\mathrm{YJHK_s}$.
2. VHS-SGC (South Galactic Cap): $b < -30^\circ$; $\delta < 1.0^\circ$ ($\sim$7000 $\mathrm{deg}^2$); excluding the VIKING SGC region and VMC region. $\mathrm{JHK_s}$ for 120 secs over VHS-DES region on the assumption that Dark Energy Survey (DES) project will project provide matching Y and Z waveband observations. This is defined as the VHS-DES region and is $4500^2$ in sky area. The DES footprint is defined below. $\mathrm{YJHK_s}$ for 60secs over the remainder of the SGC starting with the region to be covered with the VST ATLAS survey (note that some the VST-ATLAS survey lies within the VHS-DES footprint). This region is the SGC part of the VHS-ATLAS.
3. VHS-GPS (Galactic Plane Survey): as described above.

The proposed footprint (circa 2007) of the Dark Energy Survey(DES) consisted of three connected regions in the SGC.

- 20hrs $< \alpha <$ 7hrs; $-65^\circ < \delta < -30^\circ$ and 19hrs $< \alpha <$ 20hrs; $-65^\circ < \delta < -45^\circ$; $4000\,\mathrm{deg}^2$; South Pole Telescope(SPT) survey region
- 1.3hrs $< \alpha <$ 3.4hrs; $-65^\circ < \delta < -30^\circ$; $800\,\mathrm{deg}^2$
- 20.6hrs $< \alpha <$ 3.4hrs; $-1^\circ < \delta < 1^\circ$; $200\,\mathrm{deg}^2$; SDSS Stripe82

Each tile is observed in multiple wavebands in the same observing blocks (OBs) with an on-sky time execution time per OB of 360 seconds to 1080 seconds. The area of VHS-DES footprint is assumed to be 4500 $\mathrm{deg}^2$ out of the full DES footprint of 5000 $\mathrm{deg}^2$ since part of VIKING survey footprint overlaps with the DES footprint as shown in Figure 1.

In Period 89, following consultation with the PSP we changed the observing strategy in order to increase the exposure time in the bluest wavebands in the DES and ATLAS components and removed the H band observations from these OBs. This reduced the execution time per OB for these OBs by 280 seconds i.e 15%. The actual on sky exposure time for future OBs is now:

1. VHS-GPS: J (60 seconds) ; $K_s$ (60 seconds)
2. VHS-ATLAS: Y(120 seconds); J (60seconds) , $K_s$ (60 seconds)
3. VHS-DES: J (240 seconds), $K_s$ (120 seconds)

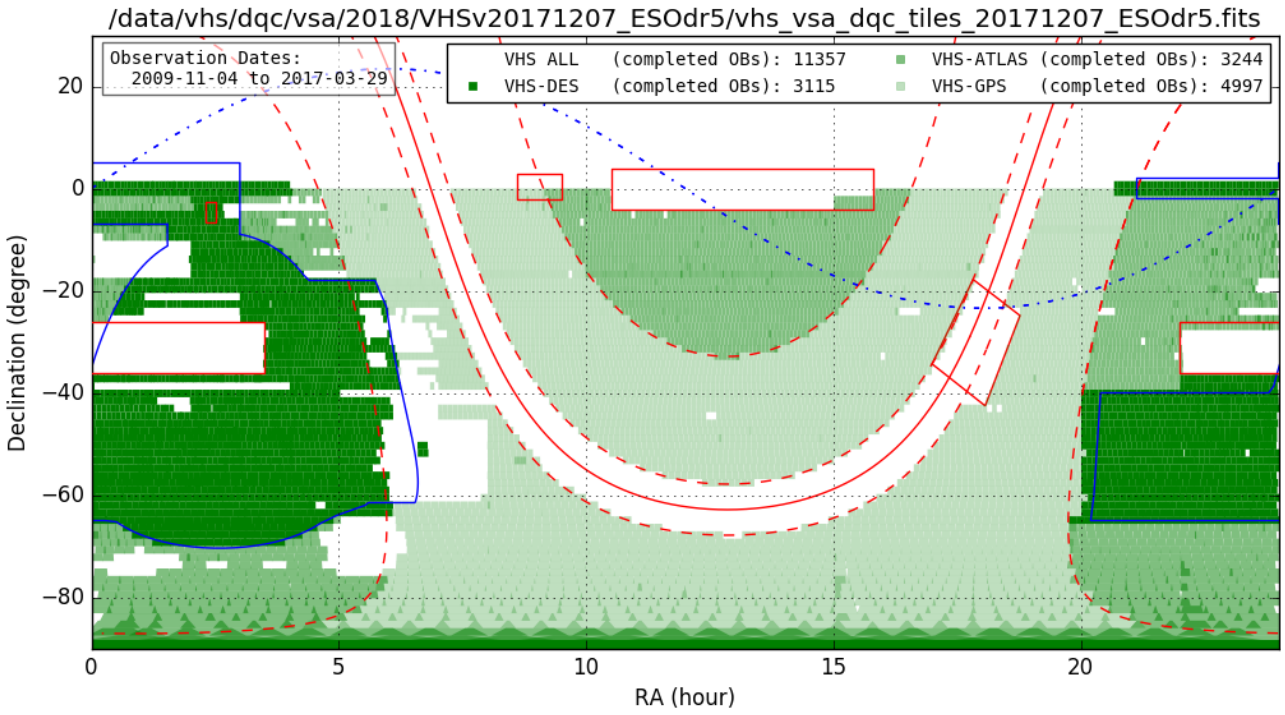


Figure 1: Sky coverage for this data release showing the total area covered (around 16,730 deg$^2$) in at least one filter as green rectangles. The blue polygon shows the DES footprint. The thick red dashed and continuous lines show galactic latitude of b=-30°, -5°, +5°, +30°. The red rectangles show the nominal VISTA VIKING and VISTA VVV survey footprints which are excluded from the VHS observations. The blue dash dotted line show the ecliptic. The legend table lists completed OB statistics for the full VHS area and for the individual survey components (i.e. DES, ATLAS and GPS).

## 2 Release Content

The sky coverage of the observations that make up this data release (DR5) is summarised in Figure 1 that plots the RA and Dec distribution of all VHS tiles observed in at least one waveband. Figures 2–5 show the coverage for each the four waveband observed in VHS; Y, J, H and $K_s$.

This data release contains data which has primarily been processed with version 1.5 of the CASU pipeline. Changes since version 1.3 of the CASU pipeline include an updated photometric calibration and updates to the Galactic extinction coefficients used in generating the photometric zero-points, together with a fix for a low-level systematic photometric variation across tile catalogues (see González-Fernández et al. (2018) for more details). The photometric recalibration, which mainly involves changes

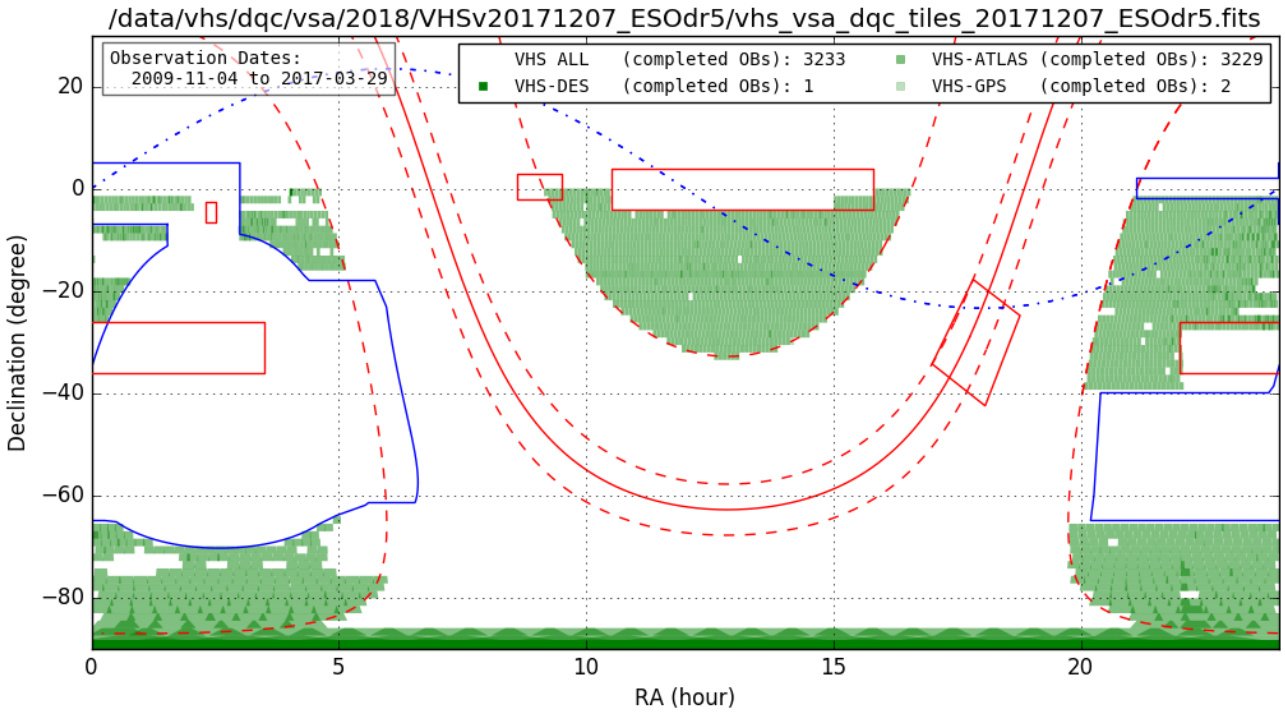


Figure 2: Sky coverage of the fields in this release in the Y waveband (4,825 deg$^2$). There are 2 OBs that are identified as GPS and 1 OB identified as a DES OB in error. See caption for Figure 1 for explanation of lines and colours.

to tile products, is being back-propagated to data taken before 2017 January 1 and these reprocessed catalogue will be published in a future data release. In most fields the zero-point change is at the level of 1% to 2%.

This data release (DR5) includes all tile level multi-band source catalogues from VHS observations taken between the start of the survey (UT date of 2009 November 04) during ESO Observing Period 84 and the end of ESO Observing Period 98 (UT date of 2017 March 31). It contains 11370 tile level multi-band catalogues based on 3226 Y band tiles, 11332 J band tiles, 1961 H band tiles and 11326 $K_s$ tiles with coverage of 4825 deg$^2$, 16689 deg$^2$, 2901 deg$^2$, 16684 deg$^2$ in Y, J, H and $K_s$ respectively. The coverage in at least one waveband is 16,730 deg$^2$ of sky. There are a total of 1,374,207,485 sources including sources detected in a single waveband.

Tile level multi-band catalogues in previous VHS releases (e.g. DR4) for observations obtained up to the end of ESO Observing Period 95 (UT date of 2015 Sep 30) are superseded by this release. Multi-band source catalogues for tiles observed before the 1st January 2017 are based on products processed with CASU pipeline version 1.3 (see Section 3.1). Multi-band source catalogues for tiles observed after 1st January 2017 used CASU pipeline version 1.5 (see Section 3.2).

This data release also includes:

1. The first public ESO release of multi-extension FITs (MEF) format pawprint image files, FITS format tile images, weight map images and single band tile source lists for ESO Observing periods 96 to 98 (UT date range 2015 October 1 to 2017 March 31 inclusive). These data products have

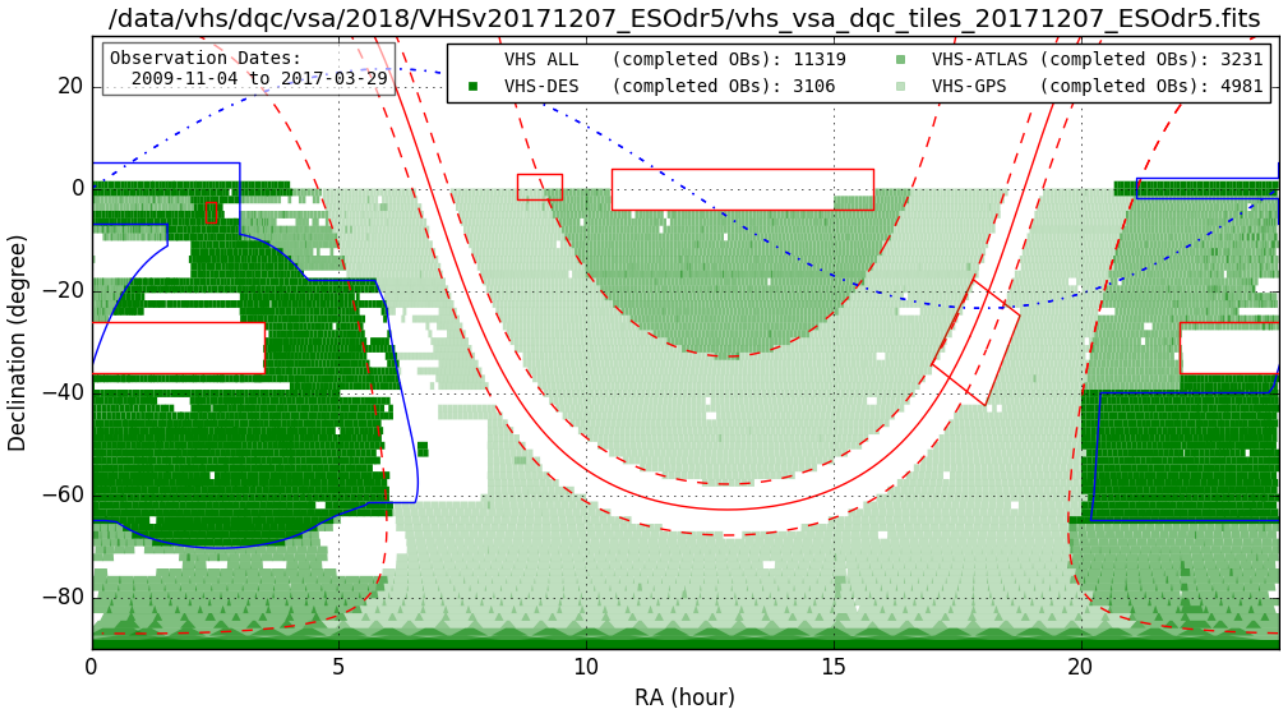


Figure 3: Sky coverage of the fields in this release in the J waveband (16,689 deg$^2$). See caption for Figure 1 for explanation of lines and colours.

all been processed by CASU pipeline version 1.5.

2. Pawprint and tile image products, and single band tile source lists for Period 95 (date range 2015 April to 2015 Sep 30) which were previously released in data release DR4, and were reprocessed with version 1.5 of the CASU software. A future date release will contain images and single source lists for observations before 2015 April (i.e. Periods 84 to 94) processed by CASU pipeline version 1.5.

Pawprint images, single band tile images and single band source list products prior to ESO Observing Period 95 are unchanged (i.e Periods 84 to 94). The FITS files have a keyword 'PROCSOFT' that specifies the version of the CASU software used. e.g. PROCSOFT = 'CASU_VIRCAM_Version_1.5' which can be used to determine the version of the CASU pipeline software used to produce a data product.

## 3 Release Notes

These release should be read in conjunction with the documentation provided at:

- CASU: http://casu.ast.cam.ac.uk/surveys-projects/vista/technical
- WFAU: http://horus.roe.ac.uk/vsa/

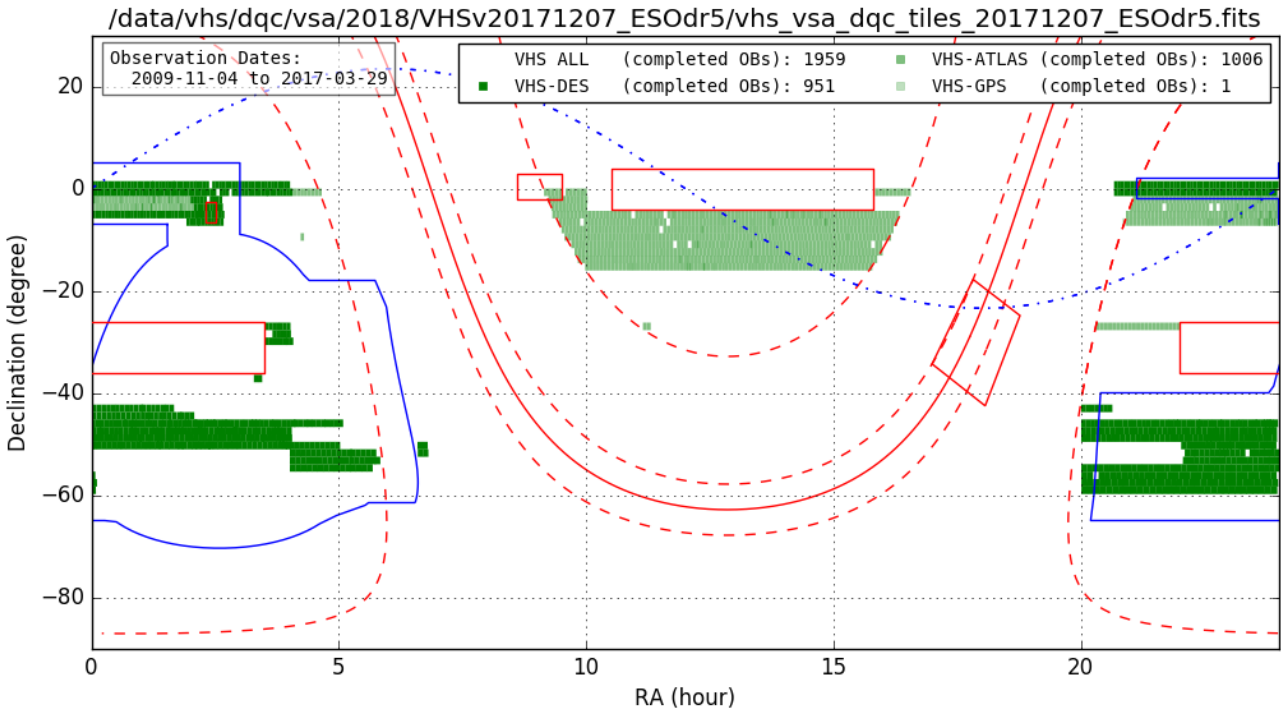


Figure 4: Sky coverage of the fields in this release in the H waveband (2,901 deg$^2$). There is currently 1 OB that is identified as a GPS OB in error. See caption for Figure 1 for explanation of lines and colours.

The CASU pipeline version 1.3 (27/03/2013) and 1.5 (observations made after 01/01/2017) are used for the data products in this release. Note that version 1.4 was used for CASU internal testing and no pipeline version 1.4 data has been released externally.

### 3.1 CASU pipeline version 1.3 (2013/03/27)

The main catalogue changes for version 1.3 are:

1. A bug involving how the aperture 2 correction was calculated is now fixed and tile catalogues have now been regrouted to include this.
2. Prior to regrouting all the stacked pawprint photometric zero-points were recomputed using the latest version of the photometry software.
3. Post regrouting all the tile photometric zero-points have also been updated.
4. ESO grades have been updated and they should now agree with those supplied by ESO to the PIs directly. This affects the keywords ESOGRADE and OBSTATUS for all data products. See the ESO Grades page for more information on their values.
5. All tile catalogues have been re-grouted taking into account both detector level magnitude zero points variations (tiles before 20101101 did not have those applied) and atmospheric seeing variations.

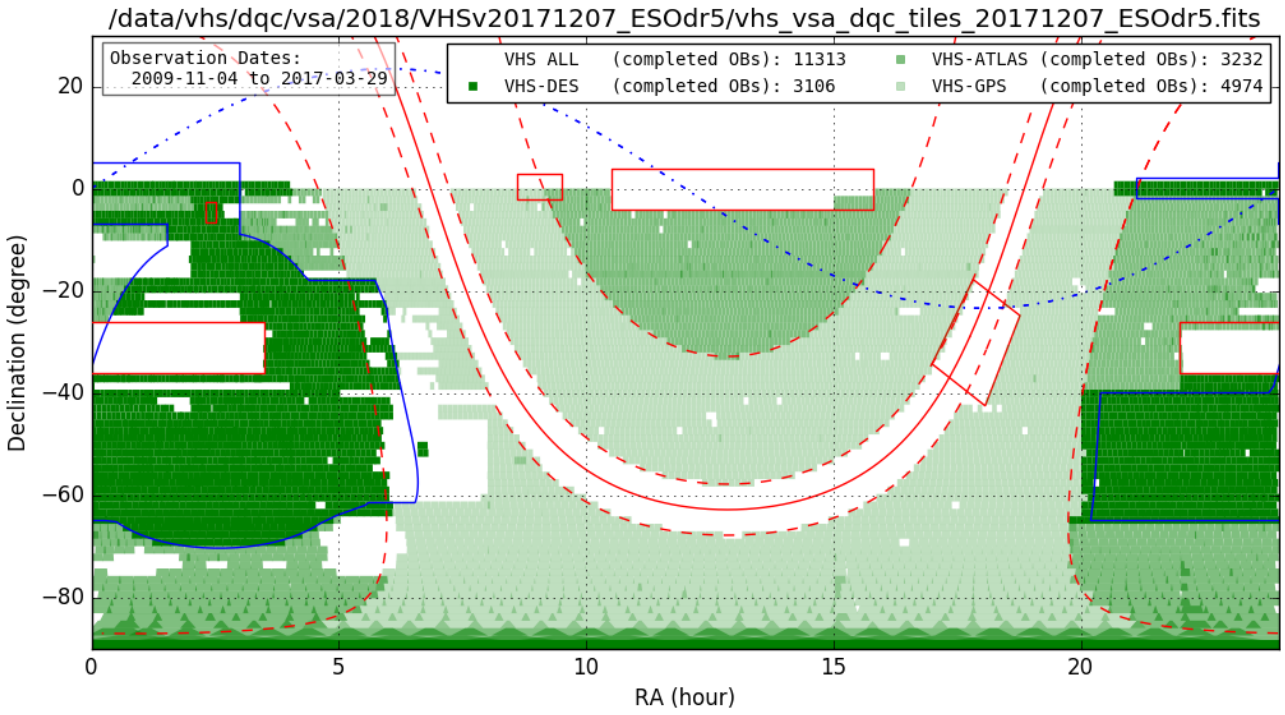


Figure 5: Sky coverage of the fields in this release in the $K_s$ waveband (16,684 deg$^2$). See caption for Figure 1 for explanation of lines and colours.

6. Note that WCS coefficients for $PV2_3$ and $PV2_5$ were changed from 42.0, - 10000.0 pre-20101130 to 44.0, -10300.0 post-20101201. The pre-20101130 astrometry was not updated.

7. The internal ZPN-TAN definition bug that affected tile products was fixed August 2012. All products post-2012801 use the corrected ZPN-TAN transformation. Earlier tile products remain affected at the ∼100mas level by this bug. All pawprint products are unaffected.

### 3.2 CASU pipeline version 1.5 (2017/01/01)

All observation taken after the start 2017 (i.e. 2017 Jan 01 onwards) have been processed with CASU pipeline version 1.5 (Note that version 1.4 was used for internal testing and no official version 1.4 data has been released externally.) Changes since version 1.3 include an updated photometric calibration and updates to the Galactic extinction coefficients used in generating the photometric zero-points, together with a fix for a low-level systematic photometric variation across tile catalogues (see González-Fernández et al. (2018) for more details). The photometric recalibration, which mainly involves changes to tile products, is being gradually back-propagated from 20161231 and will be released as it is checked out. Note that all processed pawprint images and catalogues are unchanged apart from updated magnitude zero-points. In most fields the zero-point change is at the level of 1% to 2%.

The main changes for CASU pipeline version 1.5 are:

1. Updated tile images taking account the changes in stacked pawprint zero-points.

2. Regrouted tile catalogues using photometric zero-points computed using version 1.5 of the photometry software.

3. A fix to the systematic photometry issue which affected all tile catalogues prior to 01/01/2017.

An astrometric issue at the level of 50milli arc seconds for mosaiced tile images was identified by the VHS team and presented at the ESO Surveys conference in Oct 2012. This has been fixed for tiles image data processed post-20120101. See sub-section for further information.

# 4 Data Reduction and Calibration

The data in this data release have been reduced and calibrated using with the VISTA Data Flow System as described in Irwin et al. (2004), Lewis et al. (2010) and Cross et al. (2012).

## 4.1 Data processing steps

In brief, the data processing steps are as follows:

### 4.1.1 Reset correction

This occurs in the data acquisition system, i.e. a VISTA data frame is a difference of two non-destructive detector readouts separated by DIT seconds. Then, NDIT of these frames are co-added within the data acquisition system, before saving to hard disk.

### 4.1.2 Dark subtraction

Dark subtraction uses exposures with an opaque "dark" filter inserted, with expsoure times matching the DIT values of the relevant science exposure.

### 4.1.3 Linearity correction

The VIRCAM detectors show non-linearity, typically a few percent at 10,000 ADUs (Analoge to Digital Units). A correction polynomial (one per detector) is derived from a fit to observations of the dome screen with varying exposure times and applied to the counts.

### 4.1.4 De-striping

This step removes a low-level horizontal striping intrinsic to the VIRCAM detector readout electronics, which is correlated across blocks of 4 detectors.

### 4.1.5 Flat-field correction

Each science observation image is divided by a flat-field frame, derived from a set of twilight sky flats in the matching relevant filter band.

#### 4.1.6 Bad pixel rejection

Pixels showing substantial deviance from the linearity frames are masked as bad, and assigned zero weight in subsequent combinations.

#### 4.1.7 Sky background correction

Background sky images for each wavebands are generated from all images taken for a single tile to remove large-scale background variation.

#### 4.1.8 Jitter stacking

The set of individual jittered frames for one pawprint-filter combination are combined into a pawprint image, with bad-pixel rejection. These individual pawprint images are available in the data release.

#### 4.1.9 Astrometric and Photometric calibration

This is based on matching with 2MASS (Skrutskie et al., 2006) catalogue stars (see Sections 4.2 and 4.3).

#### 4.1.10 Tiling

The six individual pawprint images for one filter are combined into a full tile image.

#### 4.1.11 Grouting

When combining images into a full tile, there are non-negligible PSF variations across the tile, due mainly to seeing variations between the six individual pawprints, and also slight variation in image quality with off-axis distance. Different pairs of pawprints contribute to different regions in the tile, thus the aperture correction varies with position. A specific correction for this (aka "grouting") is applied to the photometry in the catalogues. The effect of the grouting correction is shown in Figure 6 in González-Fernández et al. (2018).

### 4.2 Astrometric Calibration

Astrometric calibration is based on stars in the 2MASS (Skrutskie et al., 2006) catalogue; there are typically around 50 unsaturated 2MASS stars per VIRCAM pawprint detector and around 2000 per tile. The astrometric transformations from detector or tile pixel cartesian coordinates to RA, Dec are derived from these astrometric reference stars. The typical rms is 0.15 arcsec per star per coordinate, which is dominated by photon noise in the 2MASS data. 2MASS observations were obtained between 1997 June and 2001 Feb and therefore have a mean epoch of 2000. The reference frame is the International Celestial Reference System (ICRS) via the Hipparcos Tycho-2 Reference Catalog.

Figure 6 shows the distribution of the World Cooordinate System (WCS) rms astrometric errors derived from 2MASS catalogue stars. The J and $K_s$ bands have a tail to smaller rms values compared

to Y and H, since there are J and $K_s$ observations in regions of higher stellar density at lower galactic latitude ($|b| < 30°$) and shows the expected correlation between the number of stars and the rms residuals due to better determination of the WCS transformation. There is plateau in the distribution in the J and $K_s$ bands at a high stellar number density or around 4000 stars per tile. The origin is under investigation and could be a feature of sigma clipping of outliers. The horizontal feature at around 1200 stars only appears for data from P84 and P85. The origin of this effect is not currently known and reflect either a real effect in the released data or could be an issue with the DQC metadata database.

Figure 7 shows a comparison between VHS positions and the VLBI radio reference frame (Petrov (2019), http://astrogeo.org/vlbi/solutions/rfc_2019a). The results are summarized in Table 1 and compared with the results for 2MASS for the same sample of sources. The error in the systematic offsets are derived from the robust $\sigma_{MAD}$ estimator of the dispersion:

$$\sigma_{offset} = \sigma_{MAD}/\sqrt{N-1}$$

Table 1: Comparison with ICRS VLBI radio reference frame (2019a)

| Survey | Number of sources | Systematic offset | | Statistical uncertainty | |
|---|---|---|---|---|---|
| | | RA | Dec | RA | Dec |
| VHS-DR5 | 5034 | $0.005 \pm 0.002$ | $0.054 \pm 0.001$ | 0.120 | 0.095 |
| 2MASS | 4913 | $-0.002 \pm 0.002$ | $0.007 \pm 0.002$ | 0.130 | 0.133 |

## 4.3 Photometric Calibration

Photometric calibration is derived from 2MASS stars as described in González-Fernández et al. (2018). The set of colour equations are used to predict VISTA native magnitudes from the observed 2MASS J, H, $K_s$ colours. The colour equations for version 1.3 and for version 1.5 of the CASU VIRCAM pipline are given below.

### 4.3.1 CASU pipeline version 1.3 colour equations

The version 1.3 colour equations are as follows:

$$\begin{aligned} Y_V &= J_{2M} + 0.610\ (J_{2M} - H_{2M}) \\ J_V &= J_{2M} - 0.077\ (J_{2M} - H_{2M}) \\ H_V &= H_{2M} + 0.032\ (J_{2M} - H_{2M}) \\ K_{sV} &= K_{2M} + 0.01\ (J_{2M} - K_{2M}) \end{aligned}$$

where in the above, subscript 2M denotes 2MASS and V denotes VHS. The above equations give the predicted VISTA-system Vega magnitudes of 2MASS stars.

### 4.3.2 CASU pipeline version 1.5 colour equations

The version 1.5 colour equations are as follows.

$$Y_V = J_{2M} + 0.457\ (J_{2M} - K_{2M})$$
$$J_V = J_{2M} - 0.031\ (J_{2M} - K_{2M})$$
$$H_V = H_{2M} + 0.015\ (J_{2M} - K_{2M})$$
$$K_{sV} = K_{2M} - 0.006\ (J_{2M} - K_{2M})$$

In biggest change between version 1.3 and version 1.5 is the use of ($J_{2M}$ - $K_{2M}$) for all wavebands which González-Fernández et al. (2018) report is more stable with respect to galactic latitude as the slope of the colour term is less effected by the relative abundance of late type dwarfs as a function of galactic coordinates.

#### 4.3.3 Conversion from Vega to AB magnitudes

Note we have converted the native VISTA Vega mags to AB ($m_{AB} = m_{Vega} + C_{VegaToAB}$) using the below correction ($C_{VegaToAB}$):

1. For CASU pipeline version 1.3, $C_{VegaToAB} = (0.618, 0.937, 1.384, 1.839)$ for (Y, J, H, $K_s$) respectively (see http://casu.ast.cam.ac.uk/surveys-projects/vista/technical/filter-set).
2. For CASU pipeline version 1.5, $C_{VegaToAB} = (0.600, 0.916, 1.366, 1.827)$ for (Y, J, H, $K_s$) respectively (see González-Fernández et al., 2018, Appendix D).

### 4.4 Star-galaxy classification

A star-galaxy classification parameter (ClassStat) is provided in the list files; this is intended to be approximately Gaussian N(0,1) for stellar objects, and extends to large positive values for galaxies. Also an integer-based classification (Class); see description below. The band-merged catalogue file contains also merged statistics based on a quasi-Bayesian combination of the single-band classifications.

## 5 Multi-band source catalogue description

The tile level multi-band source catalogues are created from the cross-matching of single band source lists. This cross-matching band merging process is outlined in more detail in the VSA documentation and Cross et al. (2012) but involves the creation of a `vhsSource` table from the individual `vhsDetection` tables. The matching iterates through the catalogues for each band in turn (bluer to redder) and matches can include any combination of filters (one to four from Y, J, H, $K_s$) depending on how many filters it is detected in.

These single band source list tables are linked via source list reference ID numbers. The matching is done within a default radius of 2.0 arcsec and the selection between multiple potential matches can be made using the `priOrSec` (primary or secondary) flag. The `PRIMARY_SOURCE` flag has been added to provide an indication which one of the duplicates created in overlap regions between tiles should be used. The user is advised to consult with the VSA documentation and Cross et al. (2012) for more details about these flags and the band merging process.

Table 2 describes a subset of the parameters in the multi-band source catalogue tables as given in the VSA database. A description of all the columns in the multi-band source catalogues delivered in this release with their UCDs is given in Table 4.

We recommend that users should restrict their analysis to objects with `yppErrBits, jppErrBits, etc`<255 at all times and `yppErrBits`=0 if they require the most reliable subset of the sources. Values of `yppErrBits`=16 indicate that the source was deblended, `yppErrBits`=64 that at least one bad pixel was within the default aperture and `yppErrBits`=128 that the source was low confidence within the default aperture.

Table 2: A summary of the most relevant parameters in the band-merged multi-band source catalogues

| | |
|---|---|
| `ra, dec`: | RA, Dec in J2000 decimal degrees. |
| `ra, dec`: | RA, Dec in J2000 decimal degrees. |
| `l, b`: | Galactic coordinates, decimal degrees. |
| `yXi, yEta, etc`: | Source offsets from master position in each of the four bands Y, Y, H, $K_s$; in arcsec East and North respectively. |
| `priOrSec`: | Integer flag for "primary" or "secondary" source. Objects with priOrSec = 0 are unique to this tile. Objects with priOrSec = frameSetID are "primary" objects on this tile, with a secondary detection on another tile. Objects with priOrSec>0 and priOrSec != framesetID are "secondary" objects with a "primary" detection on a different tile. |
| `ySeqNum, jSeqNum, etc`: | Sequence number, enabling matching this entry to the corresponding single-band detection. |
| `ymjPnt, jmhPnt, hmksPnt`: | Respectively colours Y-J, J-H, H-$K_s$ assuming a point source, from the corresponding AperMag3 values. |
| `ymjExt, jmhExt, hmksExt`: | Respectively colours Y-J, J-H, H-$K_s$ assuming an extended source (using 2 arcsec aperture with no aperture correction). |
| `yAperMag3, yAperMag4, yAperMag6, yAperMagNoAperCorr3, yPetroMag, ySerMag, yPsfMag, etc`: | A subset of the various magnitude measures for all the single passbands, beginning with one of y,j,h,ks denoting passband. Here, a subset is given to reduce line length: of the many AperMagN values, only AperMag3,4,6 are given here, and the corresponding versions without aperture correction. |
| `yClass, yClassStat, etc`: | Respectively integer and real classification flag for each of the single bands. |
| `mergedClass, mergedClassStat`: | Band-merged integer and real classification, based on a quasi-Bayesian combination of the individual passbands. |
| `pStar, pGalaxy`: | Probability that the object is stellar/galaxy, respectively. |
| `pNoise, pSaturated`: | Probability that the object is noise/saturated, respectively. |
| `yppErrBits, jppErrBits, etc`: | Integer error bits code for each of Y, J, H, $K_s$ bands. Value Zero = no warnings, 1-255 indicates "Warning" level, and any `ppErrBits` value >256 indicates potentially more serious problems. |
| `PRIMARY_SOURCE` | Integer flag to select between multiple entries in the catalogue. If the value is 1 then this is the 'primary' entry for the source, i.e. priOrSec=0 or priOrSec=frameSetID. If the value is 0 then that entry is a duplicated source, usually a source in an overlap region between fields or tiles. |

# 6 Data quality

## 6.1 Survey Depth

The 5-sigma point source sensitivity (AB magnitudes) are given in Table 3 for each ESO observing period and each survey component. See Section 4.3 for information on the conversion of the VIRCAM

natural magnitude system which is on the Vega system to the AB magnitude system. The depth versus cumulative area per band for all observations and for each survey component is shown in Figure 8. The median $5\sigma$ point source depths for the total survey area in this data release is AB=21.1, 20.8, 20.5, 20.0 in Y, J, H and $K_s$ wavebands respectively.

Table 3: 5-sigma point source sensitivity (AB magnitudes)

| | ATLAS | | | | DES | | | GPS | | All | | | |
|---|---|---|---|---|---|---|---|---|---|---|---|---|---|
| Period | Y | J | H | $K_s$ | J | H | $K_s$ | J | $K_s$ | Y | J | H | $K_s$ |
| 84 | 20.92 | 20.84 | 20.43 | 20.00 | 21.17 | 20.77 | 20.43 | 20.76 | 19.96 | 20.91 | 20.86 | 20.69 | 20.05 |
| 85 | 20.77 | 20.72 | 20.26 | 20.08 | 21.19 | 20.78 | 20.46 | 20.56 | 19.98 | 20.77 | 21.00 | 20.26 | 20.07 |
| 86 | 20.67 | 20.68 | 20.22 | 19.95 | 21.01 | 20.52 | 20.31 | 20.42 | 19.78 | 20.67 | 20.71 | 20.43 | 20.00 |
| 87 | 20.79 | 20.73 | 20.25 | 19.93 | 21.23 | 20.77 | 20.39 | 20.56 | 19.82 | 20.79 | 20.74 | 20.55 | 19.96 |
| 88 | 20.91 | 20.75 | 20.34 | 19.99 | 21.15 | 20.71 | 20.36 | 20.86 | 20.01 | 20.91 | 20.96 | 20.54 | 20.15 |
| 89 | 21.38 | 20.96 | 20.55 | 20.10 | 21.55 | - | 20.40 | 20.79 | 19.85 | 21.38 | 20.97 | 20.55 | 20.08 |
| 90 | 21.42 | 20.89 | - | 20.01 | 21.47 | - | 20.33 | 20.87 | 19.96 | 21.42 | 21.26 | - | 20.22 |
| 91 | 21.13 | 20.66 | - | 19.96 | 21.53 | - | 20.35 | 20.69 | 19.94 | 21.13 | 20.86 | - | 20.02 |
| 92 | 21.24 | 20.80 | - | 19.98 | 21.37 | - | 20.21 | 20.61 | 19.87 | 21.24 | 20.84 | - | 19.96 |
| 93 | 21.27 | 20.84 | - | 20.00 | - | - | - | 20.74 | 21.00 | 21.27 | 20.78 | - | 19.98 |
| 94 | 21.20 | 20.71 | - | 19.81 | 21.57 | - | 20.25 | 20.70 | 19.86 | 21.20 | 20.82 | - | 19.93 |
| 95 | 21.18 | 20.77 | - | 19.92 | 21.35 | - | 20.16 | 20.60 | 19.84 | 21.18 | 20.66 | - | 19.86 |
| 96 | 21.12 | 20.66 | - | 19.84 | 21.40 | - | 20.21 | 20.60 | 19.72 | 21.12 | 20.67 | - | 19.78 |
| 97 | 21.09 | 20.68 | - | 19.84 | 21.61 | - | 20.30 | 20.55 | 19.77 | 21.09 | 20.66 | - | 19.82 |
| 98 | 21.07 | 20.71 | - | 19.78 | 21.50 | - | 20.26 | 20.52 | 19.65 | 21.07 | 20.90 | - | 19.90 |
| All | 21.13 | 20.80 | 20.31 | 19.98 | 21.41 | 20.73 | 20.33 | 20.65 | 19.87 | 21.13 | 20.82 | 20.52 | 19.99 |

***Note***: The method to compute the magnitude limits uses a `MANGLE` mask (Hamilton & Tegmark, 2004, Swanson et al., 2008) to take account the overlap between tiles.

### 6.2 Image seeing

The seeing cumulative distributions over the number of tiles is shown Figure 9.

### 6.3 Tile level spatial astrometric systematics

Figure 10 shows analysis of tile level astrometric systematics from a comparison with stacked residuals from 2MASS stars. There is a systematic effect due to an internal ZPN→TAN definition WCS bug that was fixed for tiles with date of observation after 20120801 which is during ESO observing period 89. All products of observations post-2012801 use the corrected ZPN→TAN transformation. Earlier tile products remain affected at the ∼100mas level by this bug. Pawprint products are unaffected by this WCS bug.

### 6.4 Other known problems

In the current release, the most common source of spurious images is associated with diffraction halos and filter-reflection ghosts around bright stars; these are localised around the parent star, and are easily

recognised in the parent images. There are also occasional single-band linear features from artificial satellite trails, meteors or aircraft, which can cause a chain of spurious images. Most such spurious images do not match-up between passbands, therefore multi-band matched detections are generally reliable (especially with 2 or more bands), but we emphasise that **all single-band detections should be treated as unreliable,** unless verified by inspection of images.

There are also "bad patches" on certain detectors, namely a large region on Detector#16 (South-East corner) which does not flat-field well, and a strip along an edge of detector#12 which likewise does not correct well and leads to occasional horizontal lines of spurious images.

Cross-talk between detector channels is essentially negligible.

Image persistence (latent images after a bright star lands on a pixel) is generally small, but not quite negligible: since VIRCAM has no shutter, very bright stars can occasionally cause curved "streaks" of persistence as they move in non-straight paths during telescope offsets.

There are a small number (<100) sources in the single band and band-merged catalogs that have very large (>100mag) errors due to them being close to the detection limit. These sources should be flagged manually and will be excluded in future releases. However, given they are so rare (<0.0006% of the band-merged sources) they should not be a major contaminant in any VHS study.

# 7 Acknowledgements

Any publication making use of this data, whether obtained from the ESO archive or via third parties, must include the following acknowledgment:

"Based on data products created from observations collected at the European Organisation for Astronomical Research in the Southern Hemisphere under ESO programme 179.A-2010 and made use of data from the VISTA Hemisphere survey (McMahon et al., 2013) with data pipeline processing with the VISTA Data Flow System (Irwin et al., 2004, Lewis et al., 2010, Cross et al., 2012)"

If the access to the ESO Science Archive Facility services was helpful for you research, please include the following acknowledgment:

"This research has made use of the services of the ESO Science Archive Facility. Science data products from the ESO archive may be distributed by third parties, and disseminated via other services, according to the terms of the Creative Commons Attribution 4.0 International license. Credit to the ESO origin of the data must be acknowledged, and the file headers preserved."

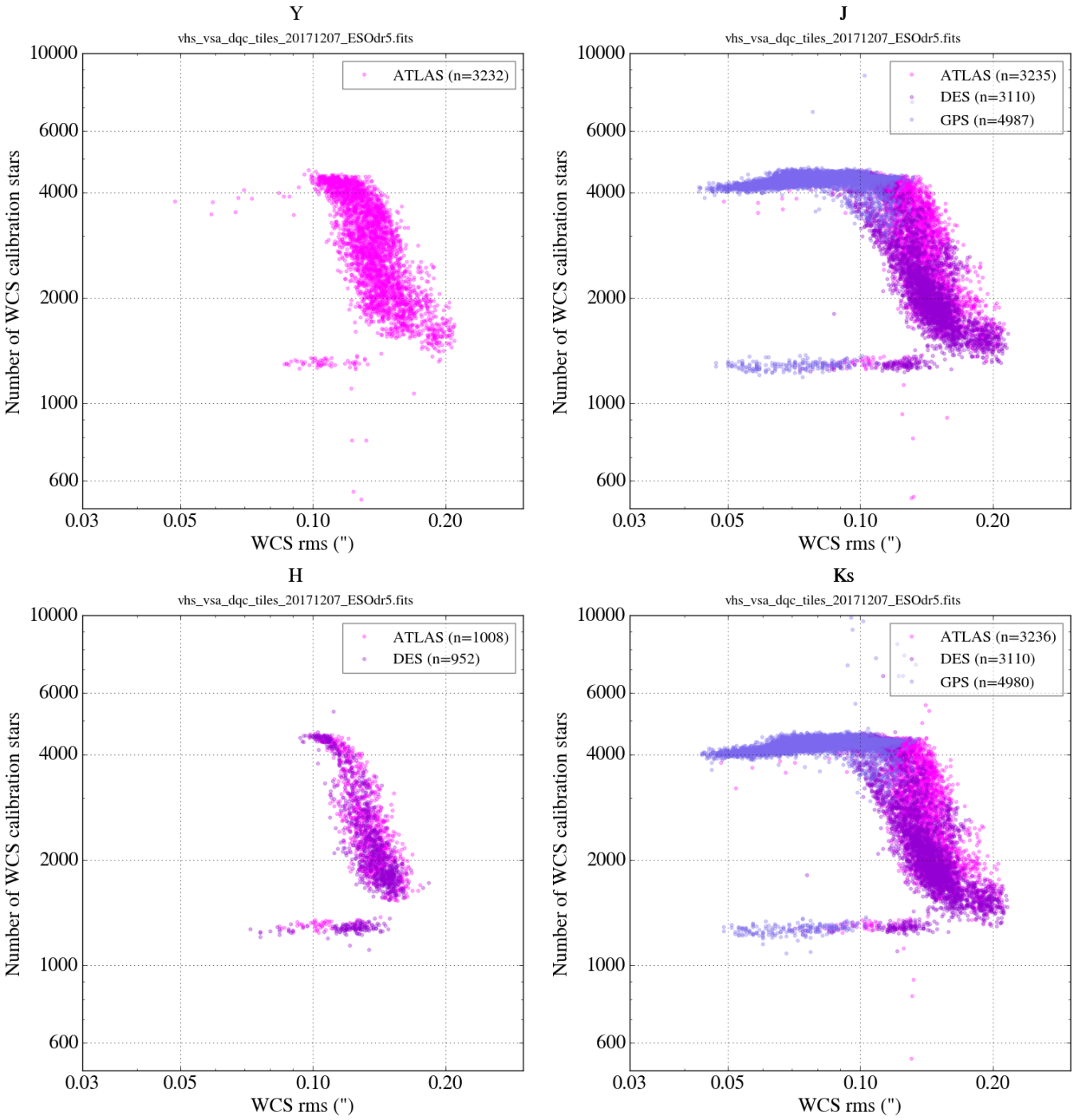


Figure 6: World Cooordinate System (WCS) rms astrometric errors versus number of 2MASS stars used for the WCS fits for tiles. This shows a correlation between the number of stars and the rms residual as expected due to fitting accuracy minimisation. The upper plateau at 4000 stars in the distribution in the J and $K_s$ bands due to upper threshold in number of stars used for the fit which is only reached at low galactic latitude. The horizontal feature at around 1200 stars only appears for data from P84 and P85. The origin of this effect is not currently known and reflect either a real effect in the released data or could be an issue with the casu DQC database. Data is for all tile catalogue observation in DR5.

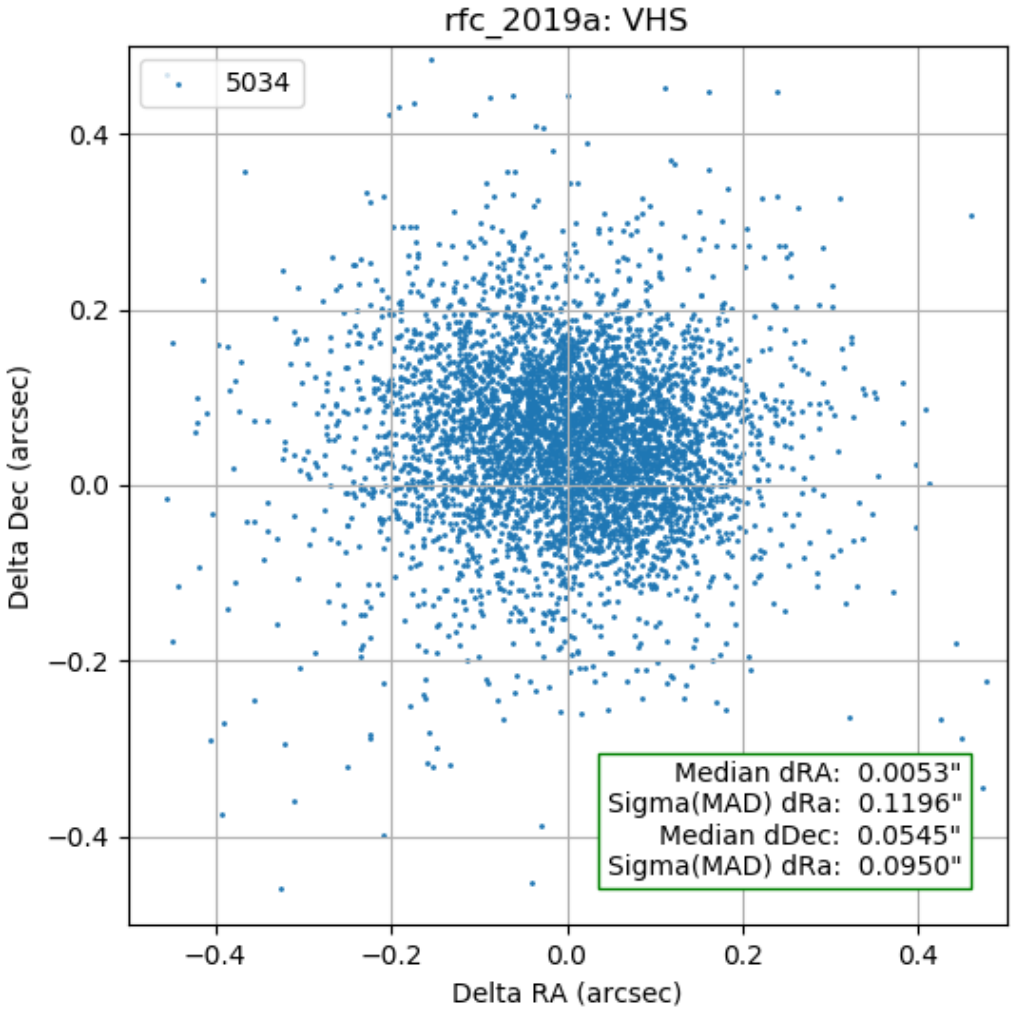


Figure 7: Comparison between VHS DR5 positions and the VLBI radio reference frame

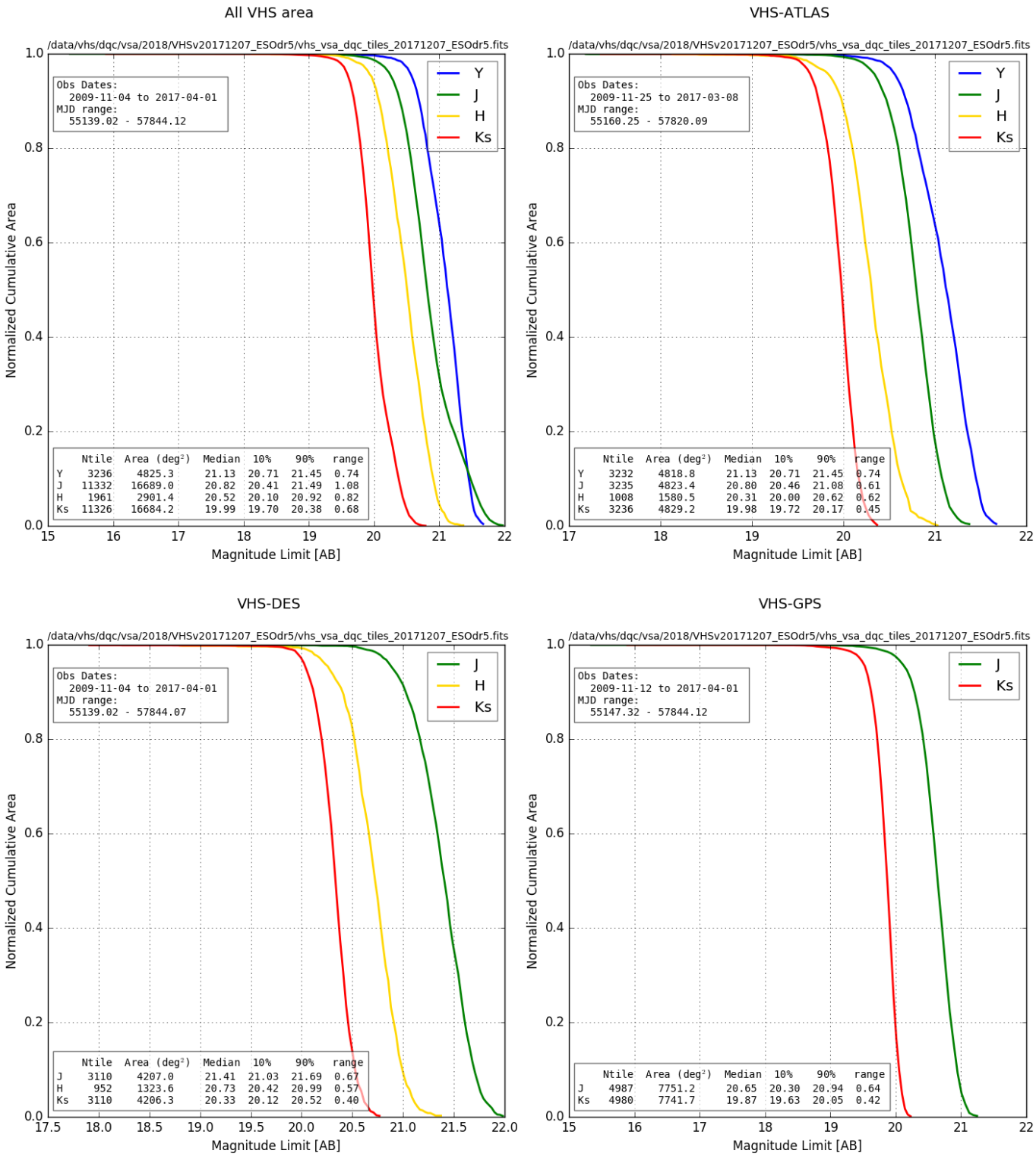


Figure 8: Depth versus cumulative area per band for all observations (top left panel) and for each survey component (ATLAS: top right panel, DES: bottom left panel and GPS: bottom right panel)

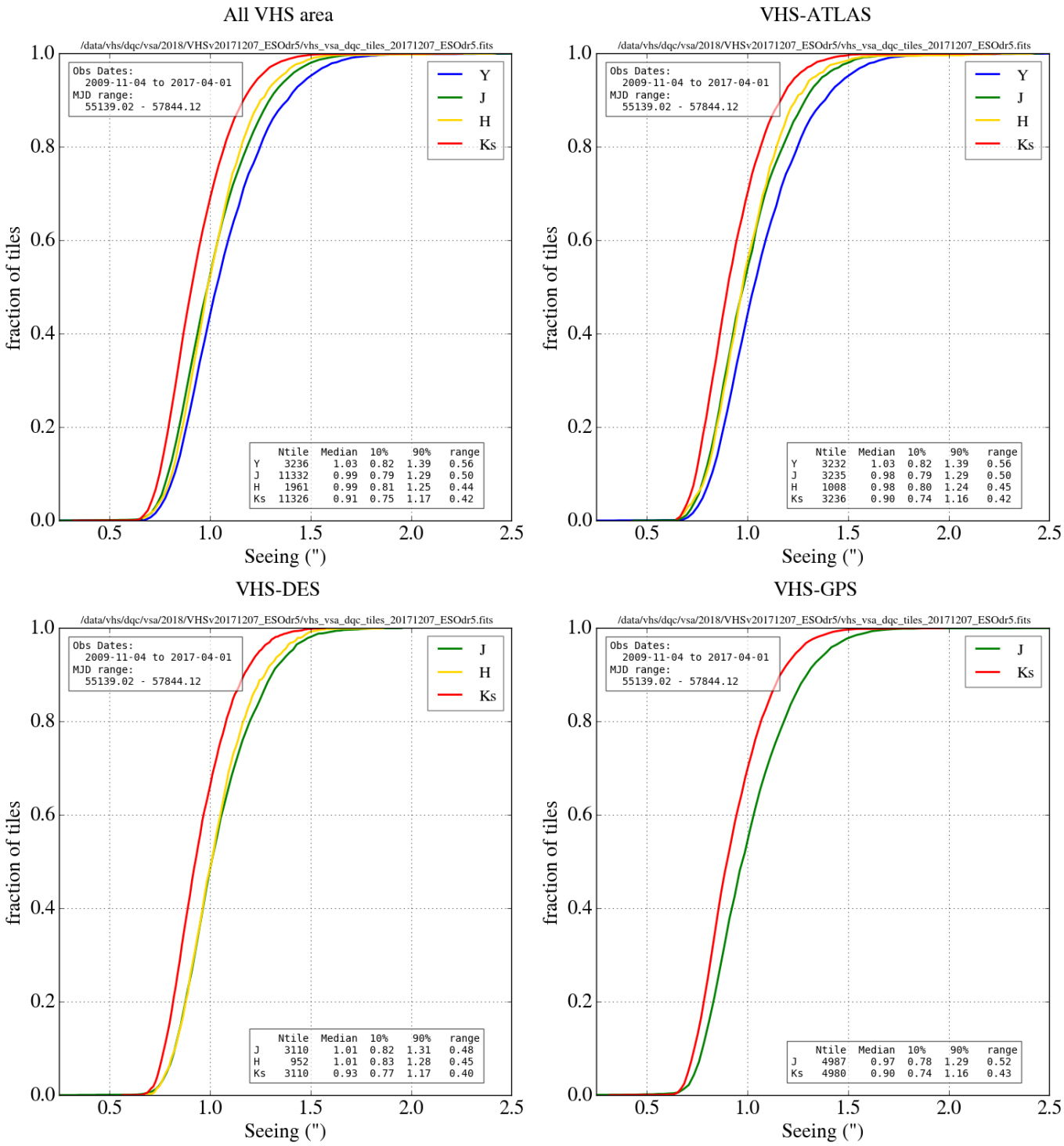


Figure 9: Seeing cumulative distribution over the number of tiles for all observations (top left panel) and for each survey component (ATLAS: top right panel, DES: bottom left panel and GPS: bottom right panel)

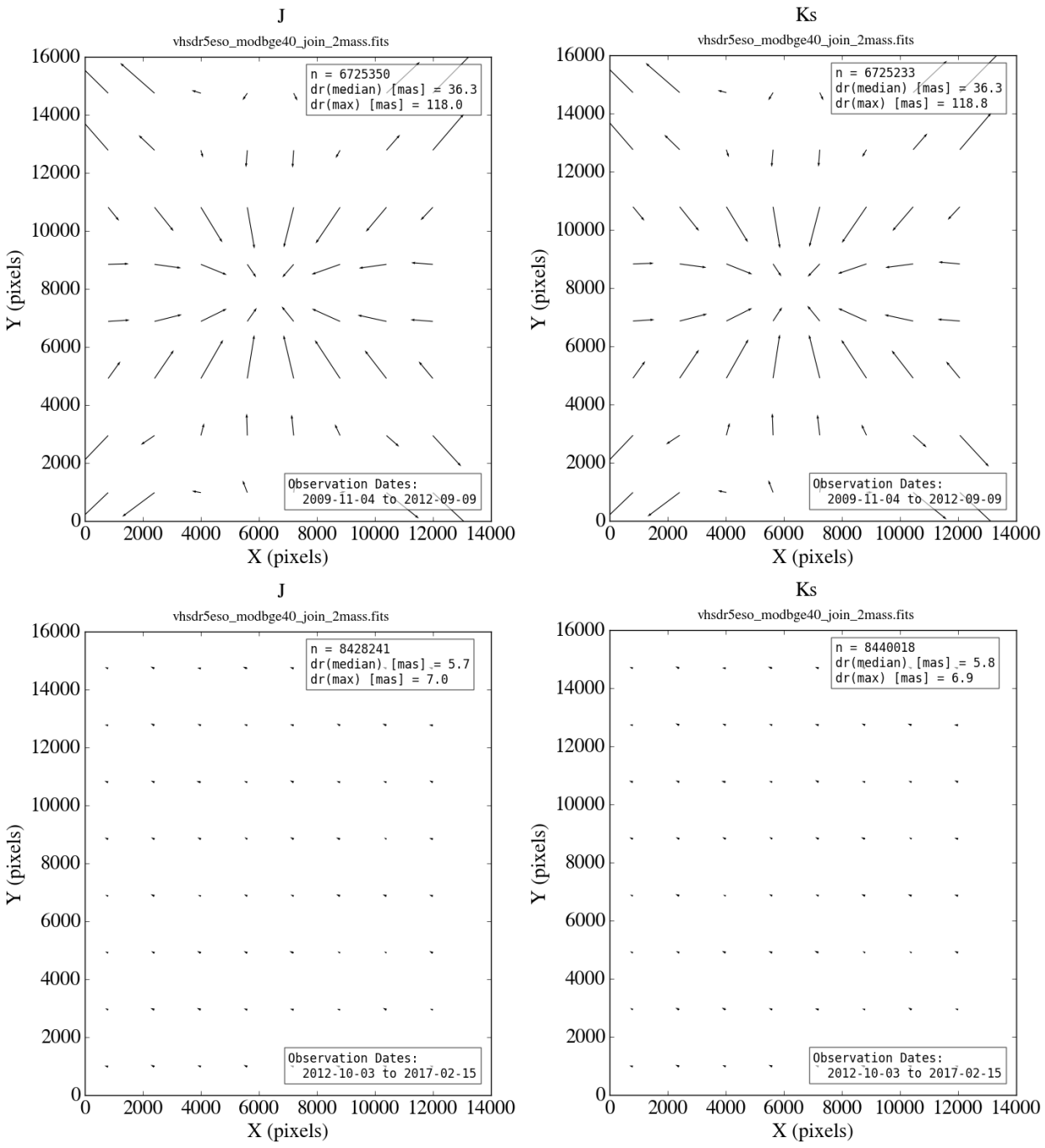


Figure 10: Analysis of Tile level systematics in astrometry from a comparison with stacked residuals from 2MASS stars. This systematic is due to an internal ZPN→TAN definition WCS bug that was fixed for tiles with date of observation after 20120801 which during ESO observing period 89. All products of observations post-20120801 use the corrected ZPN→TAN transformation. Earlier tile products remain affected at the ∼100mas level by this bug. Pawprint products are unaffected by this WCS bug.

able 4: Tile level multi-band source catalogues column names and description

| # | Column Name | Unit | Description | UCD |
|---|---|---|---|---|
| 1 | SOURCENAME | | Source name in IAU convention | meta.id |
| 2 | SOURCEID | | UID of this merged detection as assigned by merge algorithm | meta.id;meta.main |
| 3 | CUEVENTID | | UID of curation event giving rise to this record | meta.bib |
| 4 | FRAMESETID | | UID of the set of frames that this merged source comes from | meta.bib |
| 5 | RA2000 | degrees | Celestial Right Ascension | pos.eq.ra;meta.main |
| 6 | DEC2000 | degrees | Celestial Declination | pos.eq.dec;meta.main |
| 7 | L | degrees | Galactic longitude | pos.galactic.lon |
| 8 | B | degrees | Galactic latitude | pos.galactic.lat |
| 9 | LAMBDA | degrees | SDSS system spherical co-ordinate 1 | pos |
| 10 | ETA | degrees | SDSS system spherical co-ordinate 2 | pos |
| 11 | PRIORSEC | | Seam code for a unique (=0) or duplicated (!=0) source | meta.code |
| 12 | YMJPNT | mag | Point source colour Y-J (using aperMag3) | phot.color |
| 13 | YMJPNTERR | mag | Error on point source colour Y-J | stat.error |
| 14 | JMHPNT | mag | Point source colour J-H (using aperMag3) | phot.color |
| 15 | JMHPNTERR | mag | Error on point source colour J-H | stat.error |
| 16 | HMKSPNT | mag | Point source colour H-$K_s$ (using aperMag3) | phot.color |
| 17 | HMKSPNTERR | mag | Error on point source colour H-$K_s$ | stat.error |
| 18 | JMKSPNT | mag | Point source colour J-$K_s$ (using aperMag3) | phot.color |
| 19 | JMKSPNTERR | mag | Error on point source colour J-$K_s$ | stat.error |
| 20 | YMJEXT | mag | Extended source colour Y-J (using aperMagNoAperCorr3) | phot.color |
| 21 | YMJEXTERR | mag | Error on extended source colour Y-J | stat.error |
| 22 | JMHEXT | mag | Extended source colour J-H (using aperMagNoAperCorr3) | phot.color |
| 23 | JMHEXTERR | mag | Error on extended source colour J-H | stat.error |
| 24 | HMKSEXT | mag | Extended source colour H-$K_s$ (using aperMagNoAperCorr3) | phot.color |
| 25 | HMKSEXTERR | mag | Error on extended source colour H-$K_s$ | stat.error |
| 26 | JMKSEXT | mag | Extended source colour J-$K_s$ (using aperMagNoAperCorr3) | phot.color |
| 27 | JMKSEXTERR | mag | Error on extended source colour J-$K_s$ | stat.error |
| 28 | MERGEDCLASSSTAT | | Merged N(0,1) stellarness-of-profile statistic | stat |
| 29 | MERGEDCLASS | | Class flag,1\|0\|-1\|-2\|-3\|-9=gal\|noise\|star\|probStar\|probGal\|saturated | meta.code |
| 30 | PSTAR | | Probability that the source is a star | stat |
| 31 | PGALAXY | | Probability that the source is a galaxy | stat |
| 32 | PNOISE | | Probability that the source is noise | stat |
| 33 | PSATURATED | | Probability that the source is saturated | stat |
| 34 | EBV | mag | The galactic dust extinction value measured from the Schlegel maps | phys.absorption.gal |
| 35 | AY | mag | The galactic extinction correction in the Y band | phys.absorption.gal |
| 36 | AJ | mag | The galactic extinction correction in the J band | phys.absorption.gal |
| 37 | AH | mag | The galactic extinction correction in the H band | phys.absorption.gal |
| 38 | AKS | mag | The galactic extinction correction in the $K_s$ band | phys.absorption.gal |
| 39 | YMJD | days | Modified Julian Day in the Y band | time.epoch |
| 40 | YPETROMAG | mag | Extended source Y mag (Petrosian) | phot.mag;em.IR.NIR |

| | | | | |
|---|---|---|---|---|
| 41 | YPETROMAGERR | mag | Error in extended source Y mag (Petrosian) | stat.error |
| 42 | YPSFMAG | mag | Point source profile-fitted Y mag | phot.mag;em.IR.NIR |
| 43 | YPSFMAGERR | mag | Error in point source profile-fitted Y mag | stat.error |
| 44 | YSERMAG2D | mag | Extended source Y mag (profile-fitted) | phot.mag;em.IR.NIR |
| 45 | YSERMAG2DERR | mag | Error in extended source Y mag (profile-fitted) | stat.error |
| 46 | YAPERMAG3 | mag | Default point source Y aperture corrected mag (2.0 arcsec diam) | phot.mag;em.IR.NIR |
| 47 | YAPERMAG3ERR | mag | Error in default point/extended source Y mag | stat.error |
| 48 | YAPERMAG4 | mag | Point source Y aperture corrected mag (2.8 arcsec aperture diam) | phot.mag;em.IR.NIR |
| 49 | YAPERMAG4ERR | mag | Error in point/extended source Y mag (2.8 arcsec aperture diam) | stat.error |
| 50 | YAPERMAG6 | mag | Point source Y aperture corrected mag (5.7 arcsec aperture diam) | phot.mag;em.IR.NIR |
| 51 | YAPERMAG6ERR | mag | Error in point/extended source Y mag (5.7 arcsec aperture diam) | stat.error |
| 52 | YAPERMAGNOAPERCORR3 | mag | Default extended source Y aperture mag (2.0 arcsec diam) | phot.mag;em.IR.NIR |
| 53 | YAPERMAGNOAPERCORR4 | mag | Extended source Y aperture mag (2.8 arcsec aperture diameter) | phot.mag;em.IR.NIR |
| 54 | YAPERMAGNOAPERCORR6 | mag | Extended source Y aperture mag (5.7 arcsec aperture diameter) | em.IR.NIR |
| 55 | YHLCORSMJRADAS | arcsecs | Seeing corrected half-light, semi-major axis in Y band | phys.angSize |
| 56 | YGAUSIG | pixels | RMS of axes of ellipse fit in Y | src.morph.param |
| 57 | YELL | | 1-b/a, where a/b=semi-major/minor axes in Y | src.ellipticity |
| 58 | YPA | degrees | ellipse fit celestial orientation in Y | pos.posAng |
| 59 | YERRBITS | | processing warning/error bitwise flags in Y | meta.code |
| 60 | YAVERAGECONF | | average confidence in 2 arcsec diam default aperture 3 Y | stat.likelihood;em.IR.NIR |
| 61 | YCLASS | | discrete image classification flag in Y | src.class |
| 62 | YCLASSSTAT | | N(0,1) stellarness-of-profile statistic in Y | stat |
| 63 | YPPERRBITS | | additional WFAU post-processing error bits in Y | meta.code |
| 64 | YSEQNUM | | the running number of the Y detection | meta.number |
| 65 | YXI | arcsec | Offset of Y detection from master position (+east/-west) | pos.eq.ra;arith.diff |
| 66 | YETA | arcsec | Offset of Y detection from master position (+north/-south) | pos.eq.dec;arith.diff |
| 67 | JMJD | days | Modified Julian Day in the J band | time.epoch |
| 68 | JPETROMAG | mag | Extended source J mag (Petrosian) | em.IR.J |
| 69 | JPETROMAGERR | mag | Error in extended source J mag (Petrosian) | stat.error |
| 70 | JPSFMAG | mag | Point source profile-fitted J mag | em.IR.J |
| 71 | JPSFMAGERR | mag | Error in point source profile-fitted J mag | stat.error |
| 72 | JSERMAG2D | mag | Extended source J mag (profile-fitted) | em.IR.J |
| 73 | JSERMAG2DERR | mag | Error in extended source J mag (profile-fitted) | stat.error |
| 74 | JAPERMAG3 | mag | Default point source J aperture corrected mag (2.0 arcsec diam) | em.IR.J |
| 75 | JAPERMAG3ERR | mag | Error in default point/extended source J mag | stat.error |
| 76 | JAPERMAG4 | mag | Point source J aperture corrected mag (2.8 arcsec aperture diam) | em.IR.J |
| 77 | JAPERMAG4ERR | mag | Error in point/extended source J mag (2.8 arcsec aperture diam) | stat.error |
| 78 | JAPERMAG6 | mag | Point source J aperture corrected mag (5.7 arcsec aperture diam) | em.IR.J |
| 79 | JAPERMAG6ERR | mag | Error in point/extended source J mag (5.7 arcsec aperture diam) | stat.error |
| 80 | JAPERMAGNOAPERCORR3 | mag | Default extended source J aperture mag (2.0 arcsec diam) | em.IR.J |
| 81 | JAPERMAGNOAPERCORR4 | mag | Extended source J aperture mag (2.8 arcsec aperture diameter) | em.IR.J |
| 82 | JAPERMAGNOAPERCORR6 | mag | Extended source J aperture mag (5.7 arcsec aperture diameter) | em.IR.J |
| 83 | JHLCORSMJRADAS | arcsecs | Seeing corrected half-light, semi-major axis in J band | phys.angSize |

| | | | | | |
|---|---|---|---|---|---|
| 84 | JGAUSIG | pixels | RMS of axes of ellipse fit in J | | src.morph.param |
| 85 | JELL | | 1-b/a, where a/b=semi-major/minor axes in J | | src.ellipticity |
| 86 | JPA | degrees | ellipse fit celestial orientation in J | | pos.posAng |
| 87 | JERRBITS | | processing warning/error bitwise flags in J | | meta.code |
| 88 | JAVERAGECONF | | average confidence in 2 arcsec diam default aperture 3 J | | stat.likelihood;em.IR.NIR |
| 89 | JCLASS | | discrete image classification flag in J | | src.class |
| 90 | JCLASSSTAT | | N(0,1) stellarness-of-profile statistic in J | | stat |
| 91 | JPPERRBITS | | additional WFAU post-processing error bits in J | | meta.code |
| 92 | JSEQNUM | | the running number of the J detection | | meta.number |
| 93 | JXI | arcsec | Offset of J detection from master position (+east/-west) | | pos.eq.ra;arith.diff |
| 94 | JETA | arcsec | Offset of J detection from master position (+north/-south) | | pos.eq.dec;arith.diff |
| 95 | HMJD | days | Modified Julian Day in the H band | | time.epoch |
| 96 | HPETROMAG | mag | Extended source H mag (Petrosian) | | em.IR.H |
| 97 | HPETROMAGERR | mag | Error in extended source H mag (Petrosian) | | stat.error |
| 98 | HPSFMAG | mag | Point source profile-fitted H mag | | em.IR.H |
| 99 | HPSFMAGERR | mag | Error in point source profile-fitted H mag | | stat.error |
| 100 | HSERMAG2D | mag | Extended source H mag (profile-fitted) | | em.IR.H |
| 101 | HSERMAG2DERR | mag | Error in extended source H mag (profile-fitted) | | stat.error |
| 102 | HAPERMAG3 | mag | Default point source H aperture corrected mag (2.0 arcsec diam) | | em.IR.H |
| 103 | HAPERMAG3ERR | mag | Error in default point/extended source H mag | | stat.error |
| 104 | HAPERMAG4 | mag | Point source H aperture corrected mag (2.8 arcsec aperture diam) | | em.IR.H |
| 105 | HAPERMAG4ERR | mag | Error in point/extended source H mag (2.8 arcsec aperture diam) | | stat.error |
| 106 | HAPERMAG6 | mag | Point source H aperture corrected mag (5.7 arcsec aperture diam) | | em.IR.H |
| 107 | HAPERMAG6ERR | mag | Error in point/extended source H mag (5.7 arcsec aperture diam) | | stat.error |
| 108 | HAPERMAGNOAPERCORR3 | mag | Default extended source H aperture mag (2.0 arcsec diam) | | em.IR.H |
| 109 | HAPERMAGNOAPERCORR4 | mag | Extended source H aperture mag (2.8 arcsec aperture diameter) | | em.IR.H |
| 110 | HAPERMAGNOAPERCORR6 | mag | Extended source H aperture mag (5.7 arcsec aperture diameter) | | em.IR.H |
| 111 | HHLCORSMJRADAS | arcsecs | Seeing corrected half-light, semi-major axis in H band | | phys.angSize |
| 112 | HGAUSIG | pixels | RMS of axes of ellipse fit in H | | src.morph.param |
| 113 | HELL | | 1-b/a, where a/b=semi-major/minor axes in H | | src.ellipticity |
| 114 | HPA | degrees | ellipse fit celestial orientation in H | | pos.posAng |
| 115 | HERRBITS | | processing warning/error bitwise flags in H | | meta.code |
| 116 | HAVERAGECONF | | average confidence in 2 arcsec diam default aperture 3 H | | stat.likelihood;em.IR.NIR |
| 117 | HCLASS | | discrete image classification flag in H | | src.class |
| 118 | HCLASSSTAT | | N(0,1) stellarness-of-profile statistic in H | | stat |
| 119 | HPPERRBITS | | additional WFAU post-processing error bits in H | | meta.code |
| 120 | HSEQNUM | | the running number of the H detection | | meta.number |
| 121 | HXI | arcsec | Offset of H detection from master position (+east/-west) | | pos.eq.ra;arith.diff |
| 122 | HETA | arcsec | Offset of H detection from master position (+north/-south) | | pos.eq.dec;arith.diff |
| 123 | KSMJD | days | Modified Julian Day in the $K_s$ band | | time.epoch |
| 124 | KSPETROMAG | mag | Extended source $K_s$ mag (Petrosian) | | em.IR.K |
| 125 | KSPETROMAGERR | mag | Error in extended source $K_s$ mag (Petrosian) | | stat.error |
| 126 | KSPSFMAG | mag | Point source profile-fitted $K_s$ mag | | em.IR.K |

| | | | | |
|---|---|---|---|---|
| 127 | KSPSFMAGERR | mag | Error in point source profile-fitted $K_s$ mag | stat.error |
| 128 | KSSERMAG2D | mag | Extended source $K_s$ mag (profile-fitted) | em.IR.K |
| 129 | KSSERMAG2DERR | mag | Error in extended source $K_s$ mag (profile-fitted) | stat.error |
| 130 | KSAPERMAG3 | mag | Default point source $K_s$ aperture corrected mag (2.0 arcsec diam) | em.IR.K |
| 131 | KSAPERMAG3ERR | mag | Error in default point/extended source $K_s$ mag | stat.error |
| 132 | KSAPERMAG4 | mag | Point source $K_s$ aperture corrected mag (2.8 arcsec aperture diam) | em.IR.K |
| 133 | KSAPERMAG4ERR | mag | Error in point/extended source $K_s$ mag (2.8 arcsec aperture diam) | stat.error |
| 134 | KSAPERMAG6 | mag | Point source $K_s$ aperture corrected mag (5.7 arcsec aperture diam) | em.IR.K |
| 135 | KSAPERMAG6ERR | mag | Error in point/extended source $K_s$ mag (5.7 arcsec aperture diam) | stat.error |
| 136 | KSAPERMAGNOAPERCORR3 | mag | Default extended source $K_s$ aperture mag (2.0 arcsec diam) | em.IR.K |
| 137 | KSAPERMAGNOAPERCORR4 | mag | Extended source $K_s$ aperture mag (2.8 arcsec aperture diameter) | em.IR.K |
| 138 | KSAPERMAGNOAPERCORR6 | mag | Extended source $K_s$ aperture mag (5.7 arcsec aperture diameter) | em.IR.K |
| 139 | KSHLCORSMJRADAS | arcsecs | Seeing corrected half-light, semi-major axis in $K_s$ band | phys.angSize |
| 140 | KSGAUSIG | pixels | RMS of axes of ellipse fit in $K_s$ | src.morph.param |
| 141 | KSELL | | 1-b/a, where a/b=semi-major/minor axes in $K_s$ | src.ellipticity |
| 142 | KSPA | degrees | ellipse fit celestial orientation in $K_s$ | pos.posAng |
| 143 | KSERRBITS | | processing warning/error bitwise flags in $K_s$ | meta.code |
| 144 | KSAVERAGECONF | | average confidence in 2 arcsec diam default aperture 3 $K_s$ | stat.likelihood;em.IR.NIR |
| 145 | KSCLASS | | discrete image classification flag in $K_s$ | src.class |
| 146 | KSCLASSSTAT | | N(0,1) stellarness-of-profile statistic in $K_s$ | stat |
| 147 | KSPPERRBITS | | additional WFAU post-processing error bits in $K_s$ | meta.code |
| 148 | KSSEQNUM | | the running number of the $K_s$ detection | meta.number |
| 149 | KSXI | arcsec | Offset of $K_s$ detection from master position (+east/-west) | pos.eq.ra;arith.diff |
| 150 | KSETA | arcsec | Offset of $K_s$ detection from master position (+north/-south) | pos.eq.dec;arith.diff |
| 151 | PRIMARY_SOURCE | | Flag indicates primary sources (=1), otherwise (=0) | meta.code |

## References

Cross N. J. G., et al., 2012, A&A, 548, A119

Dalton G. B., et al., 2006, The VISTA infrared camera. Proc. SPIE, p. 62690X, doi:10.1117/12.670018

González-Fernández C., et al., 2018, MNRAS, 474, 5459

Hamilton A. J. S., Tegmark M., 2004, MNRAS, 349, 115

Irwin M. J., et al., 2004, VISTA data flow system: pipeline processing for WFCAM and VISTA. Proc. SPIE, pp 411–422, doi:10.1117/12.551449

Lewis J. R., Irwin M., Bunclark P., 2010, Pipeline Processing for VISTA. ASP Conf. Ser., p. 91

McMahon R. G., Banerji M., Gonzalez E., Koposov S. E., Bejar V. J., Lodieu N., Rebolo R., VHS Collaboration 2013, The Messenger, 154, 35

Skrutskie M. F., et al., 2006, , 131, 1163

Sutherland W., et al., 2015, A&A, 575, A25

Swanson M. E. C., Tegmark M., Hamilton A. J. S., Hill J. C., 2008, MNRAS, 387, 1391